

Solution-Processed Ternary Perovskite–Organic Broadband Photodetectors with Ultrahigh Detectivity

Tao Zhu, Lening Shen, Dong Zhang, Jie Zheng, and Xiong Gong*

Cite This: <https://doi.org/10.1021/acsami.2c00858>

Read Online

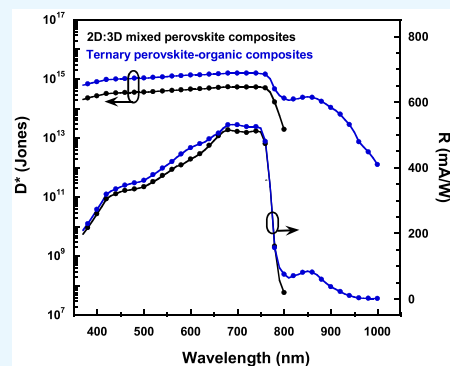
ACCESS |

Metrics & More

Article Recommendations

ABSTRACT: Room temperature operated, solution-processed ultrasensitive broadband photodetectors are widely used in various industrial companies in the scientific and medical sectors. Herein, we report solution-processed ultrahigh detectivity broadband photodetectors based on the ternary perovskite–organic composites. To ensure the photodetector based on perovskites has a photoresponse from the ultraviolet–visible to the near-infrared (NIR) region, low optical gap n-type conjugated organic molecules are incorporated with the three-dimensional (3D) perovskites mixed with the two-dimensional (2D) perovskites to form the ternary perovskite–organic composites, which possess an extended spectral response up to the NIR region and superior film characteristics compared to the 2D–3D mixed perovskite composites. Moreover, the photodetectors based on the ternary perovskite–organic composites exhibit enhanced photocurrent and suppressed dark current compared to those based on the 2D/3D mixed perovskite composites. As a result, at room temperature, the photodetectors based on the ternary perovskite–organic composites exhibit a spectral response from 375 to 1000 nm, whereas the photodetectors based on the 2D–3D mixed perovskite composites exhibit a spectral response from 375 to 800 nm. Furthermore, the photodetectors based on the ternary perovskite–organic composites have a photodetectivity over 10^{15} cm Hz^{1/2} W⁻¹ (Jones) in the ultraviolet–visible region and over 10^{13} Jones in the NIR region, a linear dynamic range over 110 dB, and a fast response time. All these results demonstrate that we developed a facile way to realize uncooled solution-processed ultrahigh detectivity broadband photodetectors based on the ternary perovskite–organic composites.

KEYWORDS: broadband photodetector, solution-processable, ternary perovskite–organic composites, extended spectral response, detectivity



INTRODUCTION

Broadband photodetectors (PDs) with spectral response from ultraviolet–visible (UV) to infrared (IR) possess an important role in military fields such as day/night vision and weapon detection, as well as civilian fields such as medical imaging, pollution detection, and meteorology.^{1–6} However, currently available IR PDs have to be operated at low temperatures (for example, at 4.2 K) to obtain reasonable sensitivities,⁵ which restrict their practical applications. Therefore, developing a multicolor PDs system with a low-cost, high quantum efficiency, and high sensitivity over the broad spectral ranges from UV to IR could be transformatively advantageous.

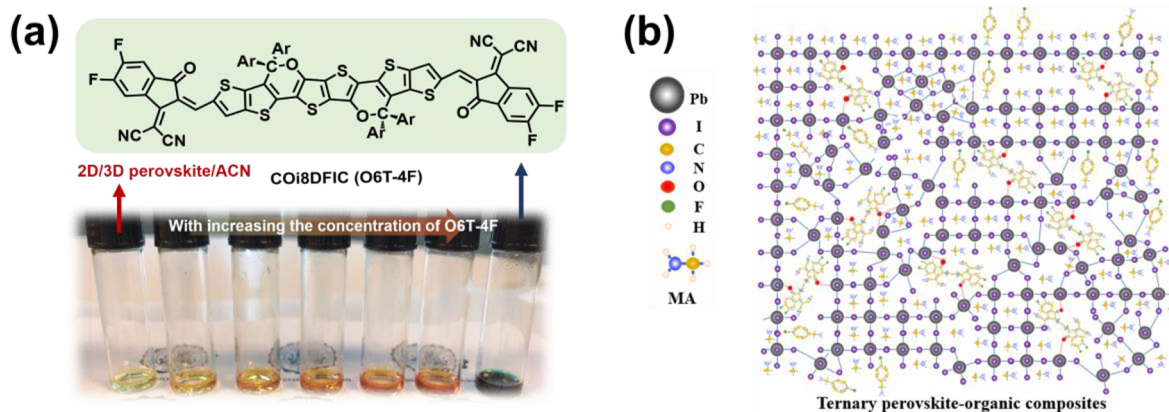
The PDs based on perovskites, taking the advantages of perovskites with effective light absorption, superior optoelectronic properties, and solution-processed manufacturing, have emerged as an alternative to realize high-performance electronics for detection applications.^{7–11} The PDs based on the three-dimensional (3D) perovskites with ultrasensitivity have been reported.^{12–15} However, the 3D perovskites are sensitive to moisture and oxygen, slowing the long-term operational stability of PDs.¹⁶ The emerging two-dimensional

(2D) perovskites incorporated with the 3D perovskites have been proven to be a simple way to approach stable perovskite photovoltaics (PPVs).^{17–20} The PPVs based on 2D incorporated with 3D perovskites with decent device performance have been reported.^{21–24} But, studies indicated that it was a challenge to boost the photocurrent of the PPVs based on 2D incorporated with 3D perovskites with decent device performance have been reported.^{21–26} But, studies indicated that it was a challenge to boost the photocurrent of the PPVs based on 2D incorporated with 3D perovskites since charge transport along the out-of-plane direction of the 2D perovskites was poor, which was attributed to the organic spacers used for creating 2D perovskites being insulators.^{21–24} Moreover, either 2D or 3D perovskites typically exhibit optical absorption in the visible

Received: February 2, 2022

Accepted: April 5, 2022

Scheme 1. (a) Molecular Structure of O6T-4F and the Picture of Perovskite Precursor Solution with Different Concentrations of O6T-4F and (b) Formation of the Ternary Perovskite-Organic Composites



region. These difficulties restricted the broadband PDs based on the 2D/3D and/or 2D/3D perovskite thin films exhibiting a broadband spectral response. Recently, we reported a novel ternary perovskite-organic composite, where low optical gap *n*-type conjugated organic molecules were incorporated with the 2D/3D mixed perovskites. These ternary composites exhibited an absorption up to the near IR (NIR) region, superior film morphology, enlarged crystallinity, enhanced and balanced charge transport, efficient photoinduced charge transfer, and dramatically suppressed the counterion movement, as compared to the 2D/3D mixed perovskite composites.²⁷ Thus, we further reported stable and efficient ternary perovskite-organic solar cells.²⁷

Here, we report solution-processed ultrahigh detectivity broadband PDs based on the ternary perovskite-organic composites that are operated at room temperature (RT). The above PDs exhibit not only extended photoresponse to the NIR region but also boosted photocurrent and suppressed dark current, as compared with those based on the 2D/3D mixed perovskites composites. Operated at RT, the above broadband PDs exhibit photodetectivity over 10^{15} Jones ($1 \text{ Jones} = 1 \text{ cm Hz}^{1/2} \text{ W}^{-1}$) in the UV–visible region and over 10^{13} Jones in the NIR region, a linear dynamic range over 110 dB, and a fast response time.

EXPERIMENTAL SECTION

Materials. γ -Butyrolactone (GBL, 99%), methylamine (MA) (33 wt % in absolute ethanol), anhydrous acetonitrile (ACN, 99.8%), poly[bis(4-phenyl)(2,4,6-trimethylphenyl)amine] (PTAA), bathocuproine (BCP, 99.99%), 4-fluorobenzylammonium (4F-BEA, 97%), molybdenum(VI) oxide (MoO_3), and Al-slug were purchased from Sigma-Aldrich. Lead iodide (PbI_2 , 99.9985% metals basis) was purchased from Alfa Aesar. C_{60} (99.95% carbon powder) was purchased from Pure C60 Olive Oil. Methylammonium iodide (MAI) was purchased from Greatcell Solar Inc. O6T-4F (also known as COi8DFIC) was purchased from One-Material Inc. All materials were directly used without any further treatment.

Thin-Film Preparation. Both 2D/3D mixed perovskites and ternary perovskite-organic composites thin films were prepared by following our previous publication.²⁷ In detail, the first step was to prepare 3D MAPbI_3 in ACN solution.²⁸ The precursor solution (PbI_2 and MAI (molar ratio 1:1) in GBL) was heated at 110°C for 3–4 h until the 3D MAPbI_3 crystals precipitated at the bottom of the vial. Considering that MA gas can infiltrate between two $[\text{PbI}_6]^{4-}$ octahedral sheets, bridging through hydrogen-bond interactions and forming the intermediate state corresponding to $\text{MA}(\text{MA})_n\text{PbI}_3$. The black 3D MAPbI_3 crystals were then dissolved into liquid perovskite

intermediate in a bottle containing methylamine GBL and ACN solution. The second step was to prepare 4F-BEA solutions, which were dissolving 4F-BEA into ACN with different concentrations. The third step was to prepare the 2D/3D mixed perovskite composite solution. A certain amount of (to adjust the ratios of 4F-BEA to the 3D MAPbI_3) 4F-BEA solution was mixed with the 3D MAPbI_3 ACN solution. The ternary perovskite-organic solution was prepared as follows: A given amount of O6T-4F solution (chosen to adjust the ratio of O6T-4F to the 2D/3D mixed perovskite composite) was mixed with the 2D/3D mixed perovskite composite solution. All thin films were prepared on substrates by the spin-casting method from the corresponding precursor solutions at 6000 rpm for 30 s and then were thermally annealed at 100°C for 10 min.

Fabrication of PDs. The fabrication of PDs is the same as those reported in our previous publications.²⁷ A $\sim 8 \text{ nm}$ PTAA thin layer was deposited on precleaned and UV-ozone treated ITO-coated glass substrates from a 2 mg mL^{-1} toluene solution, followed by thermal annealing at 100°C for 10 min, where ITO is indium tin oxide. The ternary perovskite-organic composite thin films were deposited on the top of the PTAA layer, followed again by thermal annealing at 100°C for 10 min. A $\sim 15 \text{ nm}$ C_{60} layer was then thermally deposited on top of the perovskite layer. Finally, the $\sim 8 \text{ nm}$ BCP layer and a $\sim 100 \text{ nm}$ Al layer were sequentially thermally deposited on top of the C_{60} layer in a vacuum with a base pressure of $\sim 4 \times 10^{-6}$ mbar. The device's active area was measured to be 0.043 cm^2 .

Characterization of PDs. The current densities versus voltages (*J–V*) characteristics of PDs at specific wavelengths were tested by using a Keithley model 2400 source meter with LabVIEW software. The light source was a Newport Air Mass 1.5 Global (AM1.5G) full spectrum simulator with a light intensity of 100 mW cm^{-2} . The specific wavelengths were obtained by Newport spectrum filters for giving light intensities of 0.28 and 0.16 mW cm^{-2} , respectively. The external quantum efficiency (EQE) spectrum was recorded using a solar cell quantum efficiency measurement system (QEX10). The transient photocurrent measurements were performed by using an optical chopper controlled at $\lambda = 532 \text{ nm}$ laser pulse at a frequency of 2 kHz.^{10,29}

RESULTS AND DISCUSSION

Currently, the 2D perovskite-based broadband PDs were mainly focused on the construction of double-layer binary heterostructures based on perovskites/narrow-band gap polymers or perovskites/quantum dots.^{30–36} But, the above PDs with extended spectral response were indeed demonstrated, but the multilevel utilization of photons was limited.^{30–36} Moreover, the features of poor charge transport in the out-of-plane direction and a narrow absorption range greatly render the application of the 2D perovskites in the NIR detection. Compared to the perovskite/organic bilayer thin

film, the single-layer composed of the ternary perovskite-organic composites possesses the following advantages: (1) the heterojunction system of the ternary perovskite-organic composites has a rich number of heterojunctions, which could greatly accelerate the exciton dissociation rate in the 2D perovskites, resulting in boosted charge transport of the 2D perovskites in the out-of-plane direction; (2) the introduction of low optical gap n-type conjugated organic molecules could improve the electron mobility of p-type 2D perovskites and balance charge transport; (3) through the interaction between perovskites and conjugated organic molecules, the electron energy density at the edge of the conduction band can be enhanced, the efficient transportation of electrons between conjugated organic molecules and perovskite can be assisted, and the effective utilization of the NIR absorption from low optical gap n-type conjugated organic molecules can be realized;²⁷ (4) the embedding of conjugated organic molecules could connect both the 2D and 3D perovskites, building an internal “high-speed channel” to improve the transport capacity of charge carriers in the out-of-plane direction and suppressing charge carrier recombination induced by high excitons binding energy of the 2D perovskite;²⁷ and (5) conjugated organic molecules could regulate the interface of the ternary perovskite-organic composites, resulting in improved surface morphology, reduced grain boundary defects, and suppressed dark current. Thus, we are interested in studying the PDs based on the ternary perovskite-organic composites.

Scheme 1a,b illustrates the molecular structure of O6T-4F and the illustrations of the individual components and the composites formed by the 3D MAPbI₃ (where MA is CH₃NH₃⁺) and the 2D (4F-BEA)_x(MAPbI₃)_{1-x} (where *x* is the concentration of 4F-BEA), which is referred to the 2D/3D mixed perovskite composites, and the 2D/3D mixed perovskite composites incorporated with O6T-4F, referred to the ternary perovskite-organic composites. With increasing the concentration of O6T-4F, the color of the ternary perovskite-organic composites is changed from yellowish to reddish, which is due to the formation of the ternary perovskite-organic composites (Scheme 1a). Our previous theoretical and experimental studies indicated that the chemical interactions between the O6T-4F molecules and the perovskite lattices have indeed occurred within the ternary perovskite-organic composites.²⁷ Therefore, O6T-4F molecules could be either on the surface or within the bulk of the 2D/3D mixed perovskite composites (Scheme 1b). Thin-film characteristics including the film morphology, crystal structure, charge carrier mobility, and trap densities were reported in our previous publication.²⁷ The chemical interactions between O6T-4F and perovskites are responsible for the improvement in thin film quality.²⁷

The PDs with an inverted device structure shown in Scheme 2 are fabricated. The *J*–*V* characteristics of the PDs based on either 2D/3D mixed perovskites or ternary perovskite-organic composites are shown in Figure 1a,b. At RT, the *J*–*V* characteristics of the PDs are measured in the dark and under the monochromatic light at λ of 500 nm with a light intensity of 0.28 mW cm⁻² and at λ of 800 nm with a light intensity of 0.16 mW cm⁻², respectively. At a reverse bias, the PDs based on the ternary perovskite-organic composites exhibit boosted photocurrent (*J*_{ph}) at both λ of 500 and 800 nm compared to that based on the 2D/3D mixed perovskite composites. Both PDs have a low dark current (*J*_d). Moreover, the PDs based on the ternary perovskite-organic composites exhibit more

Scheme 2. Device Structure of Photodetector, ITO/PTAA/Perovskite/C₆₀/BCP/Al, Where the Perovskite is Either the 2D/3D Mixed Perovskite or the Ternary Perovskite-Organic Composites

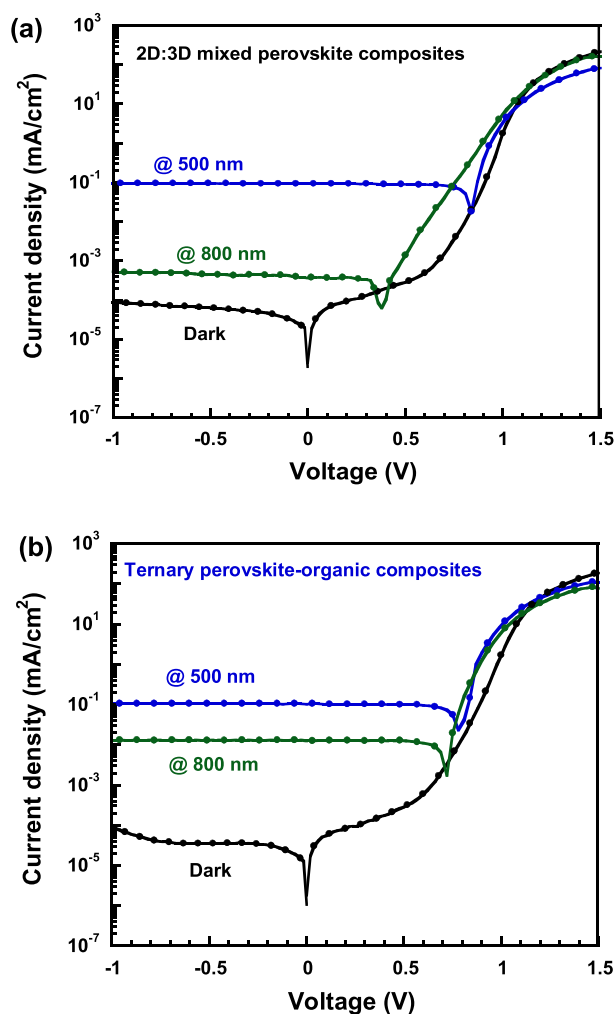
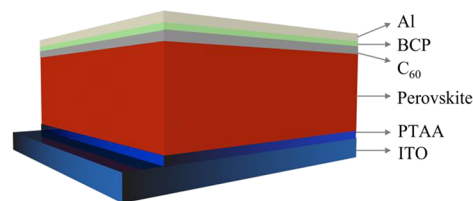


Figure 1. *J*–*V* characteristics of the perovskite-based PDs based on (a) the 2D/3D mixed perovskite composites and (b) the ternary perovskite-organic composites.

suppressed *J*_d as compared to those based on the 2D/3D mixed perovskites. For example, under a bias of -0.5 V, *J*_d of 2.88×10^{-9} mA/cm², *J*_{ph} of 8.94×10^{-2} mA/cm² at λ of 500 nm and *J*_{ph} of 4.42×10^{-4} mA/cm² at λ of 800 nm are observed from the PDs based on the 2D/3D mixed perovskite composites, whereas, *J*_d of 3.57×10^{-10} mA/cm², *J*_{ph} of 1.01×10^{-1} mA/cm² at λ of 500 nm and *J*_{ph} of 1.27×10^{-2} mA/cm² at λ of 800 nm are observed from the PDs based on the ternary perovskite-organic composites. These results indicate that the PDs based on the ternary perovskite-organic composites possess boosted detectivity compared to those based on the 2D/3D mixed perovskite composites.

Compared to the PDs based on the 2D/3D mixed perovskite composites, boosted J_{ph} observed from the PDs based on the ternary perovskite-organic composites are originated from the extended absorption range, improved film morphology, enlarged crystal sizes, enhanced and balanced charge transport, and suppressed charge recombination. Whereas, suppressed J_d observed from both PDs are probably due to a small exciton binding energy of perovskites.^{12,20,21} Furthermore, more suppressed J_d observed from the PDs based on the ternary perovskite-organic composites was ascribed to the efficient photoinduced charge transfer from perovskites to O6T-4F,²⁷ which are similar to organic-based PDs. In addition, the improved film morphology and enlarged crystallinity, balanced charge transport, and reduced trap densities are also responsible for the suppressed dark current.²⁷

In the two-terminal diodes, the saturated dark current density (J_0) is described as $J = J_0 [\exp(q(V - JR_s/nk_B T) - 1) - J_{ph}]$ (where J is the total current density, V is the applied voltage, q is the elementary electron charge, R_s is the series resistance, n is the ideal factor, k_B is the Boltzmann constant, and T is the absolute temperature).³⁷ The J_0 is directly related to the band-to-band thermal emission and charge carrier recombination in semiconductors. The $\frac{dV}{dJ}$ versus the $(J_{ph} + J)^{-1}$ is shown in Figure 2a. Thus, the R_s value for the PDs based on the ternary perovskite-organic composites is estimated to be 0.91 Ohm cm^2 , whereas the PDs based on the 2D/3D mixed perovskite composites is estimated to be 1.49 Ohm cm^2 . A smaller R_s indicates that the PDs based on the ternary perovskite-organic composites possess a high J_{ph} .³⁷ Figure 2b presents the $\ln(J_{ph} + J)$ versus the $(V - R_s J)$ and the linear fittings, which are based on the J - V characteristics of PDs (Figure 1). A J_0 of 3.57×10^{-10} mA cm^{-2} is estimated from the PDs based on the ternary perovskite-organic composites, whereas a J_0 of 2.88×10^{-9} mA cm^{-2} is estimated from the PDs based on the 2D/3D mixed perovskite composites. Thus, the PDs based on the ternary perovskite-organic composites exhibit suppressed dark current densities.

The responsivity (R), which is described as $R = \frac{J_{ph} - J_d}{P_{light}}$,^{37,38} for the PDs were further calculated. On the basis of Figure 1, R of the PDs based on the ternary perovskite-organic composites was calculated to be 361 mA/W at $\lambda = 500$ nm, whereas R for the PDs based on the 2D/3D mixed perovskite composites was calculated to be 319 mA/W. Moreover, the projected detectivity (D^*), which is described as $D^* = \frac{R}{(2qJ_d)^{1/2}}$,³⁸ was calculated. The D^* of 1.06×10^{-15} Jones (1 Jones = 1 cm $Hz^{1/2}$ W^{-1}) for the PDs based on the ternary perovskite-organic composites and the D^* of 3.32×10^{-14} Jones were calculated for the PDs based on the 2D/3D mixed perovskite composites, respectively. At a reverse bias of -0.5 V and under the monochromatic illumination of $\lambda = 800$ nm, J_{ph} values of 4.42×10^{-4} and 1.27×10^{-2} mA cm^{-2} were observed from the PDs based on the 2D/3D mixed perovskite composites and the PDs based on the ternary perovskite-organic composites, respectively. Consequently, both R of 2.76 mA/W and D^* of 3.40×10^{-12} Jones were derived for the PDs based on the 2D/3D mixed perovskite composites, and R of 79.4 mA/W and D^* of 2.34×10^{-14} Jones were derived for the PDs based on the ternary perovskite-organic composites. The significantly boosted R and D^* for the PDs based on the ternary perovskite-organic composites further confirm the contribution

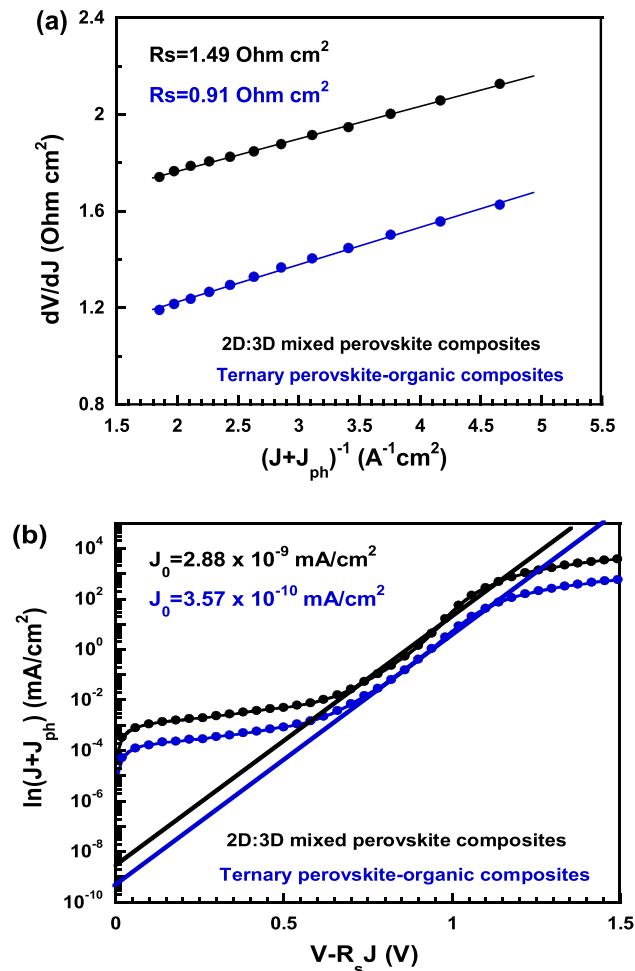


Figure 2. (a) Plot of dV/dJ versus $(J_{ph} + J)^{-1}$ and the linear fitting. (b) Plot of $\ln(J + J_{ph})$ versus $V - R_s J$ and the linear fitting of the PDs based on either 2D/3D mixed perovskite composites or the ternary perovskite-organic composites.

of O6T-4F small molecules within the ternary perovskite-organic composites. Table 1 lists the device performance parameters of PDs.

The EQE spectra (where the PDs were biased at -0.5 V) are shown in Figure 3a. The PDs based on the 2D/3D mixed perovskites composites exhibit an EQE from 375 to 800 nm, whereas the PDs based on the ternary perovskite-organic composites exhibit an EQE from 375 to 1000 nm. Figure 3b displays both R and D^* of PDs over the spectral response, which are derived on the basis of the EQE spectra and D^* at both $\lambda = 500$ nm and $\lambda = 800$ nm. At RT, the PDs based on the 2D/3D mixed perovskites possesses D^* over 10^{14} Jones only in the spectral region from 375 to 800 nm, whereas the PDs based on the ternary perovskite-organic composites possesses D^* over 10^{15} Jones from 375 to 800 nm and over 10^{13} Jones in the NIR region. These device performance parameters are better than that of silicon-based PDs.³⁹ Thus, PDs based on the ternary perovskite-organic composites exhibit a broader spectral response than that based on the 2D/3D mixed perovskite composites.

A linear dynamic range (LDR) or the photosensitivity linearity (typically quoted in dB), another typical figure of merit used to evaluate PDs device performance, was estimated according to the equation of $LDR = 20 \log(J_{ph}^*/J_d)$, where J_{ph}^* is

Table 1. Device Performance of Photodetectors^{a†}

perovskite photoactive layer	λ (nm)	J_{ph} (mA/cm ²)	J_0 (mA/cm ²)	R (mA/W)	D^* (Jones)
2D/3D mixed perovskite composites	500	8.94×10^{-2}	2.88×10^{-9}	319.00	3.32×10^{14}
	800	4.42×10^{-4}		2.76	3.40×10^{12}
ternary perovskite-organic composites	500	1.01×10^{-1}	3.57×10^{-10}	361.00	1.06×10^{15}
	800	1.27×10^{-2}		79.40	2.34×10^{14}

^{a†} J_{ph} are measured at $\lambda = 500$ nm with a light intensity of 0.28 mW/cm² and $\lambda = 800$ nm with a light intensity of 0.16 mW/cm², respectively.

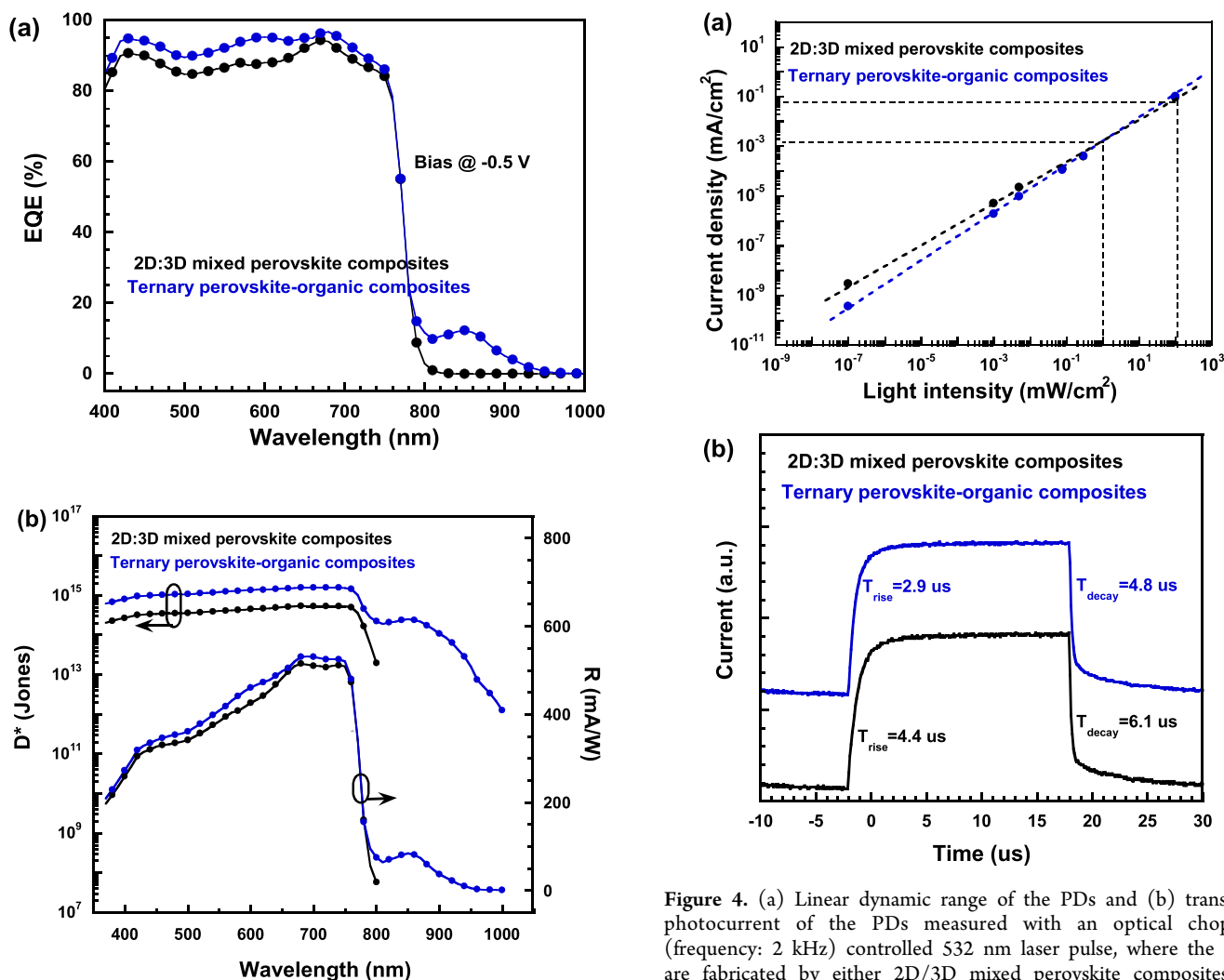


Figure 3. (a) EQE spectra of the PDs based on either 2D/3D mixed perovskite composites or ternary perovskite-organic composites. (b) Projected detectivities and responsivities versus wavelength for the PDs based on either 2D/3D mixed perovskite composites or ternary perovskite-organic composites.

the photocurrent measured at a light intensity of 1 mW cm⁻².^{2,2,38} Figure 4a displays the J_{ph} versus the light intensities for the PDs based on either 2D/3D mixed perovskite composites or ternary perovskite-organic composites. At RT, both PDs possess an LDR over 110 dB, which is much higher than that (47 dB) for the PDs based on the 3D MAPbI₃ thin film⁴⁰ and is comparable to that (120 dB, at 77K) for Si-based PDs.⁴¹

The temporal response time of PDs, an important device performance parameter reflecting PD performance, was further investigated. The rise and decay times are defined as the time to increase from 10% to 90% of the peak photocurrent and

Figure 4. (a) Linear dynamic range of the PDs and (b) transient photocurrent of the PDs measured with an optical chopper (frequency: 2 kHz) controlled 532 nm laser pulse, where the PDs are fabricated by either 2D/3D mixed perovskite composites or ternary perovskite-organic composites.

decrease from 90% to 10% of the peak photocurrent, respectively.⁴² As shown in Figure 4b, a faster rise time (2.90 μ s) and decay time (4.80 μ s) were observed from the PDs based on the ternary perovskite-organic composites, which are shorter than those observed from the PDs based on the 2D/3D mixed perovskite composites. On the basis of the Mott–Gurney law, the electron-trap densities of 1.39×10^{16} and 1.21×10^{16} cm⁻³ and the hole-trap densities of 1.09×10^{16} and 1.01×10^{16} cm⁻³ were estimated for the 2D/3D mixed perovskite composites and the ternary perovskite-organic composites, respectively.²⁷ Compared to the 2D/3D mixed perovskite composites, smaller electron-trap and hole-trap densities observed from the ternary perovskite-organic composites indicate that the ternary perovskite-organic composites possess fewer traps, which results in a faster detrapping process within the PDs based on the ternary perovskite-organic

composites. As a result, the PDs based on the ternary perovskite-organic composites possess a fast response compared to those based on the 2D/3D mixed perovskite composites.

CONCLUSIONS

In conclusion, we reported solution-processed ultrahigh detectivity broadband photodetectors based on the ternary perovskite-organic composites. Operated at room temperature, the projected detectivity of over 10^{15} Jones and the responsivity of over 300 mA/W in the visible region and the projected detectivity of over 10^{13} Jones and the responsivity of over 50 mA/W in the near-infrared region were observed from the PDs based on the ternary perovskite-organic composites. Such boosted device performance was originated from superior film morphological and optoelectronic properties of the ternary perovskite-organic composites. All these results demonstrate that we have developed a facile way to realize solution-processed ultrahigh detectivity broadband PDs based on the ternary perovskite-organic composites.

AUTHOR INFORMATION

Corresponding Author

Xiong Gong – School of Polymer Science and Polymer Engineering and Department of Chemical, Biomolecular and Corrosion Engineering, College of Engineering and Polymer Science, The University of Akron, Akron, Ohio 44325, United States; orcid.org/0000-0001-6525-3824; Email: xgong@uakron.edu; Fax: (330) 9723406

Authors

Tao Zhu – School of Polymer Science and Polymer Engineering, The University of Akron, Akron, Ohio 44325, United States

Lening Shen – School of Polymer Science and Polymer Engineering, The University of Akron, Akron, Ohio 44325, United States

Dong Zhang – Department of Chemical, Biomolecular and Corrosion Engineering, College of Engineering and Polymer Science, The University of Akron, Akron, Ohio 44325, United States; orcid.org/0000-0001-7002-7661

Jie Zheng – Department of Chemical, Biomolecular and Corrosion Engineering, College of Engineering and Polymer Science, The University of Akron, Akron, Ohio 44325, United States; orcid.org/0000-0003-1547-3612

Complete contact information is available at: <https://pubs.acs.org/10.1021/acsami.2c00858>

Notes

The authors declare no competing financial interest.

ACKNOWLEDGMENTS

The authors acknowledge the National Science Foundation (ECCS/EPMD1903303) and Air Force Office of Scientific Research (AFOSR) (through the Organic Materials Chemistry Program, Grant Number: FA9550-15-1-0292, Program Manager, Dr. Kenneth Caster) for financial support.

REFERENCES

- (1) Rogalski, A.; Antoszewski, J.; Faraone, L. Third-Generation Infrared Photodetector Arrays. *J. Appl. Phys.* **2009**, *105* (9), 091101.
- (2) Jha, A. R.; Jha, A. R.; Jha, D. A. *Infrared Technology: Applications to Electro-Optics, Photonic Devices, and Sensors*; Wiley: New York, 2000.
- (3) Rogalski, A. HgCdTe Infrared Detector Material: History, Status and Outlook. *Rep. Prog. Phys.* **2005**, *68* (10), 2267.
- (4) Tan, H.; Fan, C.; Ma, L.; Zhang, X.; Fan, P.; Yang, Y.; Hu, W.; Zhou, H.; Zhuang, X.; Zhu, X.; et al. Single-Crystalline InGaAs Nanowires for Room-Temperature High-Performance Near-Infrared Photodetectors. *Nano-Micro Lett.* **2016**, *8* (1), 29–35.
- (5) Dai, X.; Zhang, S.; Wang, Z.; Adamo, G.; Liu, H.; Huang, Y.; Couteau, C.; Soci, C. GaAs/AlGaAs Nanowire Photodetector. *Nano Lett.* **2014**, *14* (5), 2688–2693.
- (6) Keuleyan, S.; Kohler, J.; Guyot-Sionnest, P. Photoluminescence of Mid-Infrared HgTe Colloidal Quantum Dots. *J. Phys. Chem. C* **2014**, *118* (5), 2749–2753.
- (7) Im, J.-H.; Lee, C.-R.; Lee, J.-W.; Park, S.-W.; Park, N.-G. 6.5% Efficient Perovskite Quantum-Dot-Sensitized Solar Cell. *Nanoscale* **2011**, *3* (10), 4088–4093.
- (8) Stranks, S. D.; Eperon, G. E.; Grancini, G.; Menelaou, C.; Alcocer, M. J.; Leijtens, T.; Herz, L. M.; Petrozza, A.; Snaith, H. J. Electron-Hole Diffusion Lengths Exceeding 1 Micrometer in an Organometal Trihalide Perovskite Absorber. *Science* **2013**, *342* (6156), 341–344.
- (9) Xing, G.; Mathews, N.; Sun, S.; Lim, S. S.; Lam, Y. M.; Grätzel, M.; Mhaisalkar, S.; Sum, T. C. Long-Range Balanced Electron-and Hole-Transport Lengths in Organic-Inorganic $\text{CH}_3\text{NH}_3\text{PbI}_3$. *Science* **2013**, *342* (6156), 344–347.
- (10) Zhu, T.; Yang, Y.; Zheng, L.; Liu, L.; Becker, M. L.; Gong, X. Solution-Processed Flexible Broadband Photodetectors with Solution-Processed Transparent Polymeric Electrode. *Adv. Funct. Mater.* **2020**, *30* (15), 1909487.
- (11) Zheng, L.; Wang, K.; Zhu, T.; Liu, L.; Zheng, J.; Gong, X. Solution-Processed Ultrahigh Detectivity Photodetectors by Hybrid Perovskite Incorporated with Heterovalent Neodymium Cations. *ACS Omega* **2019**, *4* (14), 15873–15878.
- (12) Zhou, Y.; Chen, J.; Bakr, O. M.; Sun, H.-T. Metal-doped Lead Halide Perovskites: Synthesis, Properties, and Optoelectronic Applications. *Chem. Mater.* **2018**, *30* (19), 6589–6613.
- (13) Duong, T.; Wu, Y.; Shen, H.; Peng, J.; Fu, X.; Jacobs, D.; Wang, E. C.; Kho, T. C.; Fong, K. C.; Stocks, M.; et al. Rubidium Multication Perovskite with Optimized Bandgap for Perovskite-Silicon Tandem with Over 26% Efficiency. *Adv. Energy Mater.* **2017**, *7* (14), 1700228.
- (14) Sutton, R. J.; Eperon, G. E.; Miranda, L.; Parrott, E. S.; Kamino, B. A.; Patel, J. B.; Hörantner, M. T.; Johnston, M. B.; Haghighirad, A. A.; Moore, D. T.; et al. Bandgap-Tunable Cesium Lead Halide Perovskites with High Thermal Stability for Efficient Solar Cells. *Adv. Energy Mater.* **2016**, *6* (8), 1502458.
- (15) Xu, X.; Chueh, C. C.; Jing, P.; Yang, Z.; Shi, X.; Zhao, T.; Lin, L. Y.; Jen, A. K. Y. High-Performance Near-IR Photodetector Using Low-Bandgap $\text{MA}_{0.5}\text{FA}_{0.5}\text{Pb}_{0.5}\text{Sn}_{0.5}\text{I}_3$ Perovskite. *Adv. Funct. Mater.* **2017**, *27* (28), 1701053.
- (16) Eperon, G. E.; Stranks, S. D.; Menelaou, C.; Johnston, M. B.; Herz, L. M.; Snaith, H. J. Formamidinium Lead Trihalide: A Broadly Tunable Perovskite for Efficient Planar Heterojunction Solar Cells. *Ener. Envir. Sci.* **2014**, *7* (3), 982–988.
- (17) Tsai, H.; Nie, W.; Blancon, J.-C.; Stoumpos, C. C.; Asadpour, R.; Harutyunyan, B.; Neukirch, A. J.; Verduzco, R.; Crochet, J. J.; Tretiak, S.; et al. High-Efficiency Two-Dimensional Ruddlesden-Popper Perovskite Solar Cells. *Nature* **2016**, *536* (7616), 312–316.
- (18) Koh, T. M.; Shanmugam, V.; Schlipf, J.; Oesinghaus, L.; Müller-Buschbaum, P.; Ramakrishnan, N.; Swamy, V.; Mathews, N.; Boix, P. P.; Mhaisalkar, S. G. Nanostructuring Mixed-Dimensional Perovskites: A Route Toward Tunable, Efficient Photovoltaics. *Adv. Mater.* **2016**, *28* (19), 3653–3661.
- (19) Tian, S.; Chen, J.; Lian, X.; Wang, Y.; Zhang, Y.; Yang, W.; Wu, G.; Qiu, W.; Chen, H. Engineering the Underlying Surface to Manipulate the Growth of 2D Perovskites for Highly Efficient Solar Cells. *J. Mater. Chem. A* **2019**, *7* (23), 14027–14032.

- (20) Wang, K.; Wu, C.; Yang, D.; Jiang, Y.; Priya, S. Quasi-Two-Dimensional Halide Perovskite Single Crystal Photodetector. *ACS Nano* **2018**, *12* (5), 4919–4929.
- (21) Zhu, T.; Gong, X. Low-Dimensional Perovskite Materials and Their Optoelectronics. *InfoMat* **2021**, *3* (10), 1039–1069.
- (22) Liu, Y.; Ye, H.; Zhang, Y.; Zhao, K.; Yang, Z.; Yuan, Y.; Wu, H.; Zhao, G.; Yang, Z.; Tang, J.; et al. Surface-Tension-Controlled Crystallization for High-Quality 2D Perovskite Single Crystals for Ultrahigh Photodetection. *Matter* **2019**, *1* (2), 465–480.
- (23) Wang, J.; Li, J.; Lan, S.; Fang, C.; Shen, H.; Xiong, Q.; Li, D. Controllable Growth of Centimeter-Sized 2D Perovskite Heterostructures for Highly Narrow Dual-Band Photodetectors. *ACS Nano* **2019**, *13* (5), 5473–5484.
- (24) Dong, R.; Lan, C.; Li, F.; Yip, S.; Ho, J. C. Incorporating Mixed Cations in Quasi-2D Perovskites for High-Performance and Flexible Photodetectors. *Nanoscale Horizons* **2019**, *4* (6), 1342–1352.
- (25) Smith, I. C.; Hoke, E. T.; Solis-Ibarra, D.; McGehee, M. D.; Karunadasa, H. I. A Layered Hybrid Perovskite Solar-Cell Absorber with Enhanced Moisture Stability. *Angew. Chem.* **2014**, *126*, 11414–11417.
- (26) Cao, D. H.; Stoumpos, C. C.; Farha, O. K.; Hupp, J. T.; Kanatzidis, M. G. 2D Homologous Perovskites as Light-Absorbing Materials for Solar Cell Applications. *J. Am. Chem. Soc.* **2015**, *137*, 7843–7850.
- (27) Zhu, T.; Shen, L.; Xun, S.; Sarmiento, J. S.; Yang, Y.; Zheng, L.; Li, H.; Wang, H.; Bredas, J.-L.; Gong, X. High-Performance Ternary Perovskite-Organic Solar Cells. *Adv. Mater.* **2022**, *34* (13), 2109348.
- (28) Hou, Y.; Wu, C.; Yang, D.; Wang, K.; Ye, T.; Brownlie, L.; Wang, K.; Priya, S. Artemisinin (ART)-Induced “Perovskite/Perovskite” Bilayer Structured Photovoltaics. *Nano Energy* **2020**, *78*, 105133.
- (29) Xu, W.; Zhu, T.; Yang, Y.; Zheng, L.; Liu, L.; Gong, X. Enhanced Device Performance of Perovskite Photovoltaics by Magnetic Field-Aligned Perovskites-Magnetic Nanoparticles Composite Thin Film. *Adv. Funct. Mater.* **2020**, *30* (30), 2002808.
- (30) Tong, S. C.; Sun, J.; Wang, C. H.; Huang, Y. L.; Zhang, C. J.; Shen, J. Q.; Xie, H. P.; Niu, D. M.; Xiao, S.; Yuan, Y. B.; He, J.; Yang, J. L.; Gao, Y. L. High-Performance Broadband Perovskite Photodetectors Based on $\text{CH}_3\text{NH}_3\text{PbI}_3/\text{C}_8\text{BTBT}$ Heterojunction. *Adv. Electron. Mater.* **2017**, *3*, 1700058.
- (31) Li, C. L.; Ma, Y.; Xiao, Y. F.; Shen, L.; Ding, L. M. Advances in perovskite photodetectors. *InfoMater.* **2020**, *2*, 1247–1256.
- (32) Xu, W. Z.; Guo, Y. K.; Zhang, X. T.; Zheng, L. Y.; Zhu, T.; Zhao, D. H.; Hu, W. P.; Gong, X. Room-temperature operated ultrasensitive broadband photodetectors by perovskite incorporated with conjugated polymer and single-wall carbon nanotubes. *Adv. Funct. Mater.* **2018**, *28* (7), 1705541.
- (33) Liu, C.; Peng, H.; Wang, K.; Wei, C. D.; Wang, Z. X.; Gong, X. PbS Quantum Dots-Induced Trap-Assisted Charge Injection in Perovskite Photodetectors. *Nano Energy* **2016**, *30*, 27–35.
- (34) Liu, C.; Wang, K.; Du, P.; Wang, E.; Gong, X.; Heeger, A. J. Ultrasensitive Solution-Processed Near-Infrared Photodetectors using $\text{CH}_3\text{NH}_3\text{PbI}_3$ and PbS Quantum Dots as the Light Harvesters. *Nanoscale* **2015**, *7* (39), 16460–16469.
- (35) Zeng, L. H.; Chen, Q. M.; Zhang, Z. X.; Wu, D.; Yuan, H. Y.; Li, Y.-Y.; Qarony, W.; Lau, S. P.; Luo, L. B.; Tsang, Y. H. Multilayered PdSe_2 /Perovskite Schottky Junction for Fast, Self-Powered, Polarization-Sensitive, Broadband Photodetectors, and Image Sensor Application. *Adv. Sci.* **2019**, *6* (19), 1901134.
- (36) Zhang, J. Y.; Xu, L.; Chen, T.; Gao, X.; Wang, S. D. Toward Broadband Imaging: Surface-Engineered PbS Quantum Dot/Perovskite Composite Integrated Ultrasensitive Photodetectors. *ACS Appl. Mater. Interfaces* **2019**, *11* (47), 44430–44437.
- (37) Sze, S. M.; Ng, K. K. *Physics of semiconductor devices*; John Wiley & Sons, 2006.
- (38) Gong, X.; Tong, M.; Xia, Y.; Cai, W.; Moon, J. S.; Cao, Y.; Yu, G.; Shieh, C.-L.; Nilsson, B.; Heeger, A. J. High-Detectivity Polymer Photodetectors with Spectral Response from 300 to 1450 nm. *Science* **2009**, *325* (5948), 1665–1667.
- (39) Wojtas, J.; Tittel, F.; Stacewicz, T.; Bielecki, Z.; Lewicki, R.; Mikolajczyk, J.; Nowakowski, M.; Szabra, D.; Stefanski, P.; Tarka, J. Cavity-Enhanced Absorption Spectroscopy and Photoacoustic Spectroscopy for Human Breath Analysis. *Int. J. Thermophys.* **2014**, *35* (12), 2215–2225.
- (40) Zheng, L.; Zhu, T.; Xu, W.; Zheng, J.; Liu, L.; Gong, X. Ultrasensitive Perovskite Photodetectors by Co Partially Substituted Hybrid Perovskite. *ACS Sustainable Chem. Eng.* **2018**, *6* (9), 12055–12060.
- (41) Hegedus, S. S.; Shafarman, W. N. Thin-Film Solar Cells: Device Measurements and Analysis. *Progress in Photovoltaics: Research and Applications* **2004**, *12* (2–3), 155–176.
- (42) Xu, W.; Guo, Y.; Zhang, X.; Zheng, L.; Zhu, T.; Zhao, D.; Hu, W.; Gong, X. Room-Temperature-Operated Ultrasensitive Broadband Photodetectors by Perovskite Incorporated with Conjugated Polymer and Single-Wall Carbon Nanotubes. *Adv. Funct. Mater.* **2018**, *28* (7), 1705541.